Geophysical Journal International

Geophys. J. Int. (2016) **207,** 967–982
Advance Access publication 2016 August 15
GJI Geodynamics and tectonics

doi: 10.1093/gji/ggw308

Deep electrical resistivity tomography along the tectonically active Middle Aterno Valley (2009 L'Aquila earthquake area, central Italy)

Stefano Pucci,[1] Riccardo Civico,[1] Fabio Villani,[1] Tullio Ricci,[1] Eric Delcher,[2] Anthony Finizola,[2] Vincenzo Sapia,[1] Paolo Marco De Martini,[1] Daniela Pantosti,[1] Stéphanie Barde-Cabusson,[3] Elodie Brothelande,[4] Rachel Gusset,[2] Cécile Mezon,[2] Simone Orefice,[1] Aline Peltier,[5] Matthieu Poret,[2,6] Liliana Torres[2,7] and Barbara Suski[8]

[1] *Istituto Nazionale di Geofisica e Vulcanologia, Roma, Italy. E-mail: stefano.pucci@ingv.it*
[2] *Laboratoire GéoSciences Réunion, Université de la Réunion, Institut de Physique du Globe de Paris, Sorbonne Paris-Cité, CNRS, UMR 7154, Saint-Denis, La Réunion, France*
[3] *Departamento de Geología ambiental y georiesgos, Instituto de Ciencias de la Tierra "Jaume Almera", Barcelona, Spain*
[4] *Laboratoire Magmas et Volcans, Université Blaise Pascal-CNRS-IRD, OPGC, UMR 6524, Clermont-Ferrand, France*
[5] *Observatoire Volcanologique du Piton de la Fournaise, Institut de Physique du Globe de Paris, Sorbonne Paris Cité, CNRS, UMR 7154, Géologie des Systèmes Volcaniques, La Réunion, France*
[6] *Istituto Nazionale di Geofisica e Vulcanologia, Bologna, Italy*
[7] *Instituto Geofísico del Perú, Lima, Peru*
[8] *MEMSFIELD, Clamart, France*

Accepted 2016 August 10. Received 2016 August 10; in original form 2015 November 2

SUMMARY

Three 2-D Deep Electrical Resistivity Tomography (ERT) transects, up to 6.36 km long, were obtained across the Paganica-San Demetrio Basin, bounded by the 2009 L'Aquila M_w 6.1 normal-faulting earthquake causative fault (central Italy). The investigations allowed defining for the first time the shallow subsurface basin structure. The resistivity images, and their geological interpretation, show a dissected Mesozoic-Tertiary substratum buried under continental infill of mainly Quaternary age due to the long-term activity of the Paganica-San Demetrio normal faults system (PSDFS), ruling the most recent deformational phase. Our results indicate that the basin bottom deepens up to 600 m moving to the south, with the continental infill largely exceeding the known thickness of the Quaternary sequence. The causes of this increasing thickness can be: (1) the onset of the continental deposition in the southern sector took place before the Quaternary, (2) there was an early stage of the basin development driven by different fault systems that produced a depocentre in the southern sector not related to the present-day basin shape, or (3) the fault system slip rate in the southern sector was faster than in the northern sector. We were able to gain sights into the long-term PSDFS behaviour and evolution, by comparing throw rates at different timescales and discriminating the splays that lead deformation. Some fault splays exhibit large cumulative throws (>300 m) in coincidence with large displacement of the continental deposits sequence (>100 m), thus testifying a general persistence in time of their activity as leading splays of the fault system. We evaluate the long-term (3–2.5 Myr) cumulative and Quaternary throw rates of most of the leading splays to be 0.08–0.17 mm yr^{-1}, indicating a substantial stability of the faults activity. Among them, an individual leading fault splay extends from Paganica to San Demetrio ne' Vestini as a result of a post-Early Pleistocene linkage of two smaller splays. This 15 km long fault splay can explain the Holocene surface ruptures observed to be larger than those occurred during the 2009 L'Aquila earthquake, such as revealed by palaeoseismological investigations. Finally, the architecture of the basin at depth suggests that the PSDFS can also rupture a longer structure at the surface, allowing earthquakes larger than M 6.5, besides rupturing only small sections, as it occurred in 2009.

Key words: Electrical properties; Tectonics and landscape evolution; Neotectonics; Fractures and faults; Europe.

1 INTRODUCTION

The M_w 6.1 2009 April 6 L'Aquila earthquake and its long aftershocks sequence (Scognamiglio *et al*. 2010; Herrmann *et al*. 2011; Valoroso *et al*. 2013) struck a densely populated area in the Middle Aterno Valley (central Apennines) and caused heavy damage in the town of L'Aquila and surrounding villages, resulting in 309 fatalities and thousands of injured. As reported also by historical records (http://emidius.mi.ingv.it/CPTI; Tertulliani *et al*. 2009; Rovida *et al*. 2011) this region is one of the most active areas of Italy and was repeatedly hit by destructive earthquakes.

Seismological, geodetic and geological data all converge in identifying as the 2009 main-shock causative fault an NW–SE oriented, SW-dipping normal fault whose length is still a matter of debate as different observations and models suggest being between 12 and 18 km (e.g. Atzori *et al*. 2009; Cheloni *et al*. 2010; Cirella *et al*. 2012; Volpe *et al*. 2012). Its surface expression, known as the Paganica-San Demetrio fault system (PSDFS – *sensu* Civico *et al*. 2015), is located along the eastern flank of the Middle Aterno Valley (Fig. 1). Here, the PSDFS affects Quaternary deposits and shows composite fault scarps with throws of tens of meters and lengths of several kilometres (Civico *et al*. 2015; Pucci *et al*. 2015).

Prior to the 2009 earthquake, the geometry and activity of the PSDFS were only roughly known (see Galli *et al*. 2010 for a review). After the event, a significant number of studies have been carried out in the Middle Aterno Valley, in particular along the Paganica-San Demetrio Basin, focusing mainly on the coseismic geological surface effects, the structural setting, the geomorphology and the palaeoseismic history (Falcucci *et al*. 2009; Boncio *et al*. 2010; Emergeo Working Group 2010; Galli *et al*. 2010, 2011; Cinti *et al*. 2011; Vittori *et al*. 2011; Lavecchia *et al*. 2012; Blumetti *et al*. 2013; Moro *et al*. 2013; Santo *et al*. 2014; Civico *et al*. 2015; Pucci *et al*. 2015). There is a general discrepancy between the length of the seismologic–geodetic modelled fault (up to 18 km), the limited size of the primary continuous coseismic surface ruptures (3 km), and the significant morphological expression of the PSDFS. This stimulated a debate about the maximum rupture length of the PSDFS and its capability to generate earthquakes stronger than the 2009 main shock, with much larger rupture length and displacement. Consequently, some Authors focused on the analysis of the Quaternary geological and morphological expression of PSDFS at the surface, since it can be useful to estimate the role and rate of long-term activity of the fault system (Giaccio *et al*. 2012; Civico *et al*. 2015). With the same aim, a few works have investigated the shallow subsurface of the basin, but only in the northwestern sector (Cesi *et al*. 2010; Balasco *et al*. 2011; Improta *et al*. 2012; Santo *et al*. 2014; Fig. 2).

Moreover, the area lacks deep boreholes, extensive deep geophysical data and seismic exploration lines from oil and gas industry, thus the overall subsurface structure of the Paganica-San Demetrio Basin in its central and southeastern sectors is still uncovered.

To contribute to fill this gap of knowledge, we carried out an electrical resistivity tomography campaign across the basin, targeting the northern, central and southeastern sectors of the PSDFS, respectively. In this paper, we present the results of three 2-D Deep Electrical Resistivity Tomography (ERT) profiles that we obtained by employing a long acquisition layout with large offset of electrodes, the combined use of a remote injection electrode (in one case) and an advanced post-processing approach (details in Section 3). This methodology is a novel application for active tectonic areas and it represents an important reference for the development of similar studies elsewhere. Its application in our case allowed: (1) defining the structure of the basin bottom; (2) reaching the Mesozoic-Tertiary substratum; (3) imaging the geometry of the basin infill and of some PSDFS fault splays.

Due to the good quality of these resistivity images, we can reliably estimate the Quaternary throws of some important splays of the PSDFS and individuate the ones leading the Quaternary deformation of the area.

In the following, we present a summary of the seismotectonic setting of the area and of the available data on the structure of the Paganica-San Demetrio Basin, the applied methodology, the results and their interpretation followed by the derivative geological cross-sections.

2 THE PAGANICA-SAN DEMETRIO BASIN

The Paganica-San Demetrio Basin is a 16 km long, 3–6 km wide, intramontane basin in the central Apennines (Abruzzi region, central Italy). Along with the nearby L'Aquila basin, it is part of the Middle Aterno Valley and is bounded by a system of NW-striking normal faults. Since the Late Pliocene, normal faulting superimposes and dissects NE-verging thrust-and-fold belt that forms the bulk of the Apennines (e.g. Lavecchia *et al*. 1994; Galadini & Galli 2000; Boncio *et al*. 2004; Galadini & Messina 2004). The present-day extension is perpendicular to the chain axis (Montone *et al*. 2012 and references therein) and is estimated to be 2–3 mm yr^{-1} (Hunstad *et al*. 2003; D'Agostino *et al*. 2011). NE–SW active extension is confirmed also by focal mechanisms of the earthquakes of the last decades (Chiarabba *et al*. 2005). The 2009 L'Aquila earthquake sequence fully fits in this seismotectonic context: seismologic, geodetic, DInSar and geological data all depict the M_w 6.1 2009 April 6 main-shock causative fault as an NW–SE oriented, SW-dipping structure (Chiaraluce 2012; Vannoli *et al*. 2012 and references therein). The 2009 aftershocks are confined on a planar, single fault at depth and spread into a wider volume toward the surface (within the uppermost ∼3–4 km; Chiaraluce *et al*. 2011). The 2009 causative fault crops out and bounds the Middle Aterno Valley to the east, in coincidence with the PSDFS, where it shows a complex surface expression, with several synthetic and antithetic splays affecting the Quaternary basin continental infill (Bagnaia *et al*. 1992; Vezzani & Ghisetti 1998; Boncio *et al*. 2004; ISPRA 2006; Pucci *et al*. 2015; Figs 1 and 2). The 2009 L'Aquila earthquake produced 3 km long continuous primary coseismic ruptures that extend to a length of ∼10 km when also discontinuous and sparse ruptures are considered. Maximum throws of 0.15 m occurred along the base of a long-term, cumulative tectonic scarp of a synthetic splay of the PSDFS (Falcucci *et al*. 2009; Boncio *et al*. 2010; Emergeo Working Group 2010; Galli *et al*. 2010; Vittori *et al*. 2011; Fig. 1). The coseismic deformation field generated by the fault slip as imaged by DInSAR and GPS data sets (Anzidei *et al*. 2009; Atzori *et al*. 2009; Walters *et al*. 2009; Papanikolaou *et al*. 2010; Trasatti *et al*. 2011) shows the maximum coseismic lowering (values ranging from 0.16 to 0.27 m) located between the L'Aquila and Paganica-San Demetrio basins (Fig. 1).

The Paganica-San Demetrio basin is partially filled with sequences of Quaternary continental deposits extensively outcropping in the area and unconformably overlying a Meso-Cenozoic substratum (Bosi & Bertini 1970; Bertini & Bosi 1993; D'Agostino *et al*. 1997; Cavinato & De Celles 1999; Centamore *et al*. 2006; Giaccio *et al*. 2012; Pucci *et al*. 2015). The latter is composed of three different marly carbonatic marine sequences (ISPRA 2006; Fig. 3a):

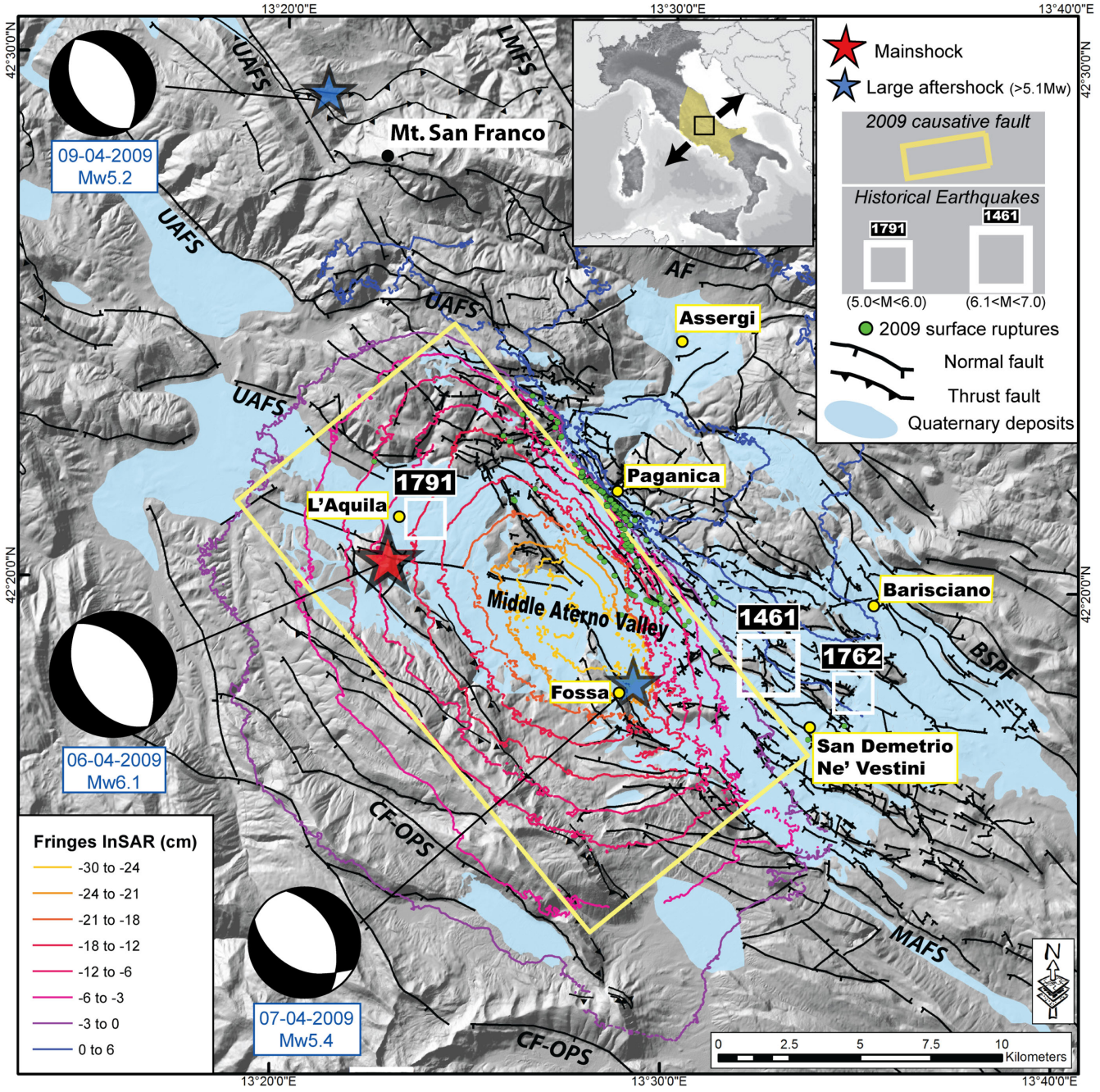

Figure 1. Location map of the 2009 L'Aquila main shock and of the two largest aftershocks ($M > 5.0$—stars; Scognamiglio *et al*. 2010; Herrmann *et al*. 2011), coseismic surface ruptures (from Emergeo Working Group 2010 and Boncio *et al*. 2010) and displacement field from DInSAR fringes (Atzori *et al*. 2009). Focal mechanism of the main shock and of the two largest aftershocks, historical seismicity ($M > 5.0$; http://emidius.mi.ingv.it/CPTI04) and main active faults are shown [UAFS: Upper Aterno Fault System; LMFS: Laga Mountain Fault System; CIFS: Campo Imperatore Fault System; AF: Assergi Fault; PSDFS: Paganica – San Demetrio Fault System; MAFS: Middle Aterno Fault System; CF-OPS: Campo Felice – Ovindoli Pezza Fault System (Galadini & Galli 2000)]. The yellow box is the approximate projection to the surface of the ∼16 km long 2009 main-shock causative fault according to various investigators (see a review in Vannoli *et al*. 2012 and Chiaraluce 2012). The inset shows the direction of extension across the central Apennines (black arrows) and the regional felt area for the 6 April main shock (www.haisentitoilterremoto.it; coloured area).

(1) the Aterno Valley-Mt. Camarda sequence, to the South, West and Southeast; (2) the Paganica sequence, to the North-East; (3) the Mt. Pettino sequence to the North, featuring also Miocene arenaceous flysch (Fig. 3a).

The Quaternary continental infill deposits that bury the substratum can be referred to three main cycles (Fig. 3b): (1) slope-derived carbonatic breccia and conglomerates, locally well-cemented, up to 100 m thick (Valle Valiano *Fm*. – VVB/VVC; Early Pleistocene); (2) fluvio-lacustrine cycle (Early Pleistocene), including whitish carbonate lacustrine silts (S. Nicandro *Fm*. - SNL) partially heteropic with deltaic conglomeratic deposits, locally cemented (Vall'Orsa *Fm*. - VOC), up to 200 m thick; (3) upper fluvio-alluvial cycle (Early-Middle Pleistocene), carved in the VVB/VVC, consisting of conglomeratic alluvial fan deposits (Valle dell'Inferno

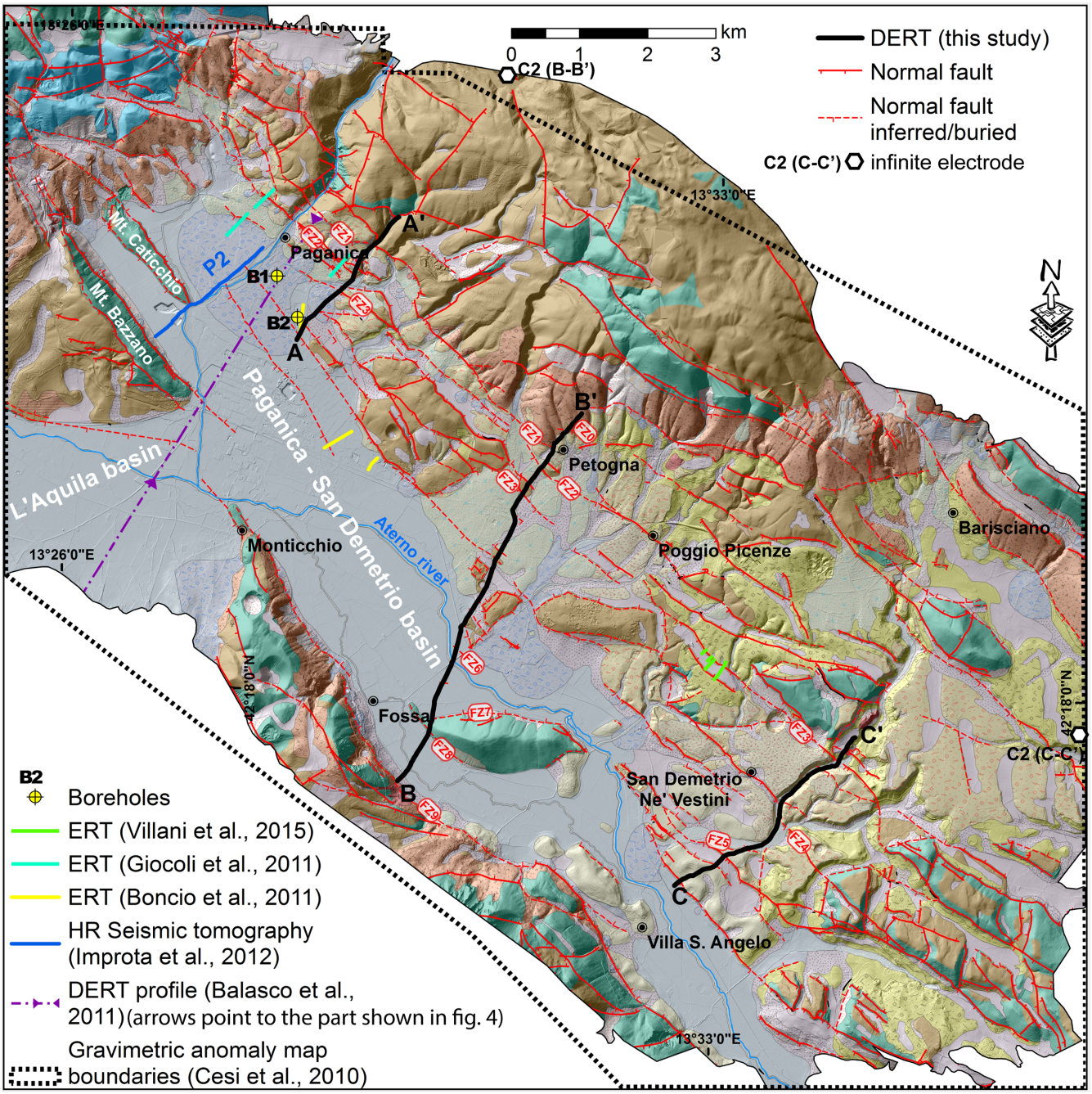

Figure 2. Geologic map of the Paganica-San Demetrio Basin area highlighting the structural arrangement of the fault system and the extent and the outcropping pre-Quaternary, Quaternary and Holocene deposits (modified after Pucci *et al*. 2015; see Fig. 3 for the geological legend). The traces of the ERT profiles of this study and their corresponding remote electrode location are shown in black along with a summary of the other post-2009 geophysical investigations. Red labels of main normal faults imaged by Deep ERTs are reported.

Fm. - VIC) overlaid by silts and sands rich in volcanic ashes with carbonate gravels (S. Mauro *Fm*. – SMA/SMF), up to 100 m thick. All these deposits are covered by Late Pleistocene (AFP)—Holocene fluvial/alluvial sandy-gravelly sediments, mainly related to the Aterno River, and by slope debris and colluvial deposits. The Quaternary continental infill exhibits complex stratigraphical relationships including large unconformities and hiatuses (Giaccio *et al*. 2012; Pucci *et al*. 2015). In particular, a generalized southward increasing thickness was observed from Paganica to Poggio Picenze and San Demetrio ne' Vestini areas (Fig. 3).

Moreover, at the basin scale, Civico *et al*. (2015) highlighted the existence of a complex structural setting of the PSDFS at the surface, characterized by several parallel fault splays frequently arranged in a quasi-fractal sequence of horst and graben of variable size (e.g. Villani *et al*. 2015). According to this work, the PSDFS comprises two main sectors: (1) the Paganica sector to the NW, characterized by a narrow deformation zone and a relatively small Quaternary basin; (2) the San Demetrio sector to the SE, characterized by a set of parallel, km-spaced fault splays that exhume and dissect a wider Quaternary basin.

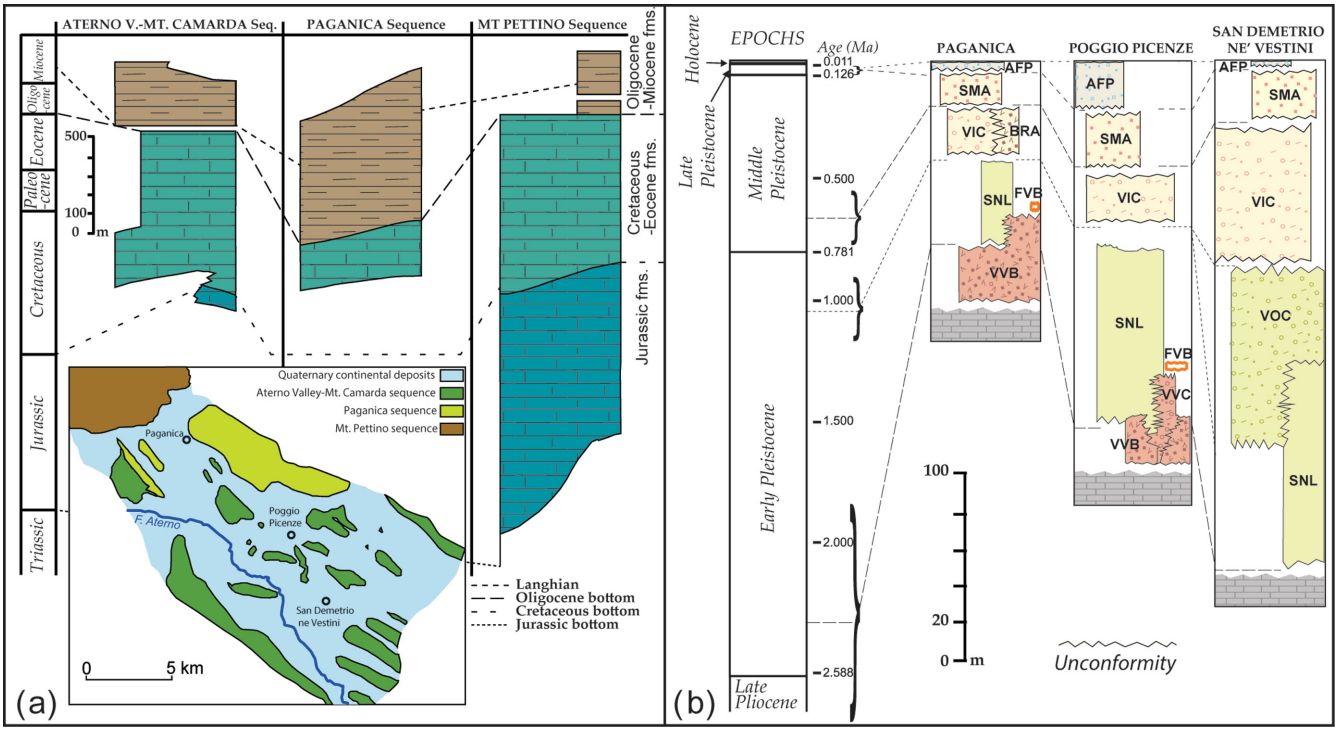

Figure 3. (a) Stratigraphic sequences of the substratum domains (modified from ISPRA 2006). The inset shows the map of the main substratum domains of the study area; (b) stratigraphic columns of the three sequences of Plio-Quaternary continental deposits filling the Paganica-San Demetrio Basin (modified after Pucci *et al*. 2015). AFP, ancient alluvial fan deposits; SMA/SMF, San Mauro, alluvial and fluvial units; VIC, Valle dell'Inferno conglomerates; VOC, Vall'Orsa conglomerates; SNL, San Nicandro lacustrine deposits; BRA, L'Aquila Breccias; FVB, Fonte Vedice breccia; VVB/VVC, Valle Valiano breccia and conglomerates. The uncertainty of their age is shown by braces.

The complex surficial stratigraphic and structural setting at the basin scale also reflects in the subsurface setting. Balasco *et al*. (2011) investigated the subsurface structure of the Middle Aterno Valley by means of a ∼8 km long, ∼1000 m deep ERT. The NE part of resistivity section (Fig. 4a) highlighted the existence of complex lateral and vertical heterogeneous resistivity areas in the NE sector (between Mt. Bazzano and Paganica), due to shallow conductive alluvial filling (up to 200 m thick) above the carbonate substratum, indicating the presence of a narrow depocentre of low-resistivity sediments close to the Paganica fault.

In addition, Cesi *et al*. (2010) produced a residual gravimetric anomaly map of the Middle Aterno Valley (Fig. 4b). This image suggests a complex structure of the entire basin, but it does not provide quantitative clues on the variable infill thickness because the lack of calibration with density data or any forward modelling of the gravimetric anomalies.

Furthermore, a ∼2 km long 2-D shallow seismic survey was performed by Improta *et al*. (2012) across the northern part of the Paganica-San Demetrio Basin, in the hanging-wall of the PSDFS (Fig. 4c). Along this transect, the tomographic images defined the basin structure down to a depth of ∼300 m, highlighting again high complexity, due to the presence of a dissected pre-Quaternary substratum, with a main ∼250 m deep depocentre in front of Mt. Bazzano and a cumulative displacement of the Paganica fault larger (>200 m) than previously inferred by surface data alone. Moreover, they evidenced the presence of strong lateral heterogeneities and steps in the substratum, suggesting the presence of buried synthetic and antithetic fault splays of the PSDFS involving bedrock and basin infill deposits.

3 ELECTRICAL RESISTIVITY TOMOGRAPHY

In order to provide a basin-wide subsurface picture down to the top of the substratum, we acquired three ERT profiles crossing orthogonally (average SW-NE trend) both the eastern edge of the Quaternary basin and the PSDFS (Fig. 2). The northern profile (ERT1, A–A′) runs for 2.52 km close to the Paganica village; the central one (ERT2, B–B′) crosses the entire basin from Fossa to Petogna villages for 6.36 km; and the southern one (ERT3, C–C′) 3.8 km long is located close to the San Demetrio ne' Vestini village. The main characteristics of the ERT profiles are summarized in Table 1.

3.1 Data acquisition

Measurements were undertaken with a multi-electrode 2D device by means of the ABEM Terrameter SAS-4000 instrument and an ABEM ES1064 C multiplexer. We used a 2.52 km long cable with a set of 64 stainless steel electrodes and offset of 40 m, subdivided in 16 reels (4 take-out per reel), as those already used by Revil *et al*. (2011). Profiles B–B′ and C–C′ required several short 'roll-along' of 1/4 of the electrodes array to cover the entire length as well as to limit the size of the interpolated area during the subsequent inversion process. The A–A′, B–B′, and C–C′ profiles have been performed respectively on May 2009, March 2014, and January 2012. Profiles were measured with different configurations: A–A′ with Wenner-alpha; B–B′ and C–C′ with both Wenner–alpha and forward and reverse pole–dipole. While using large spacing (40 m)

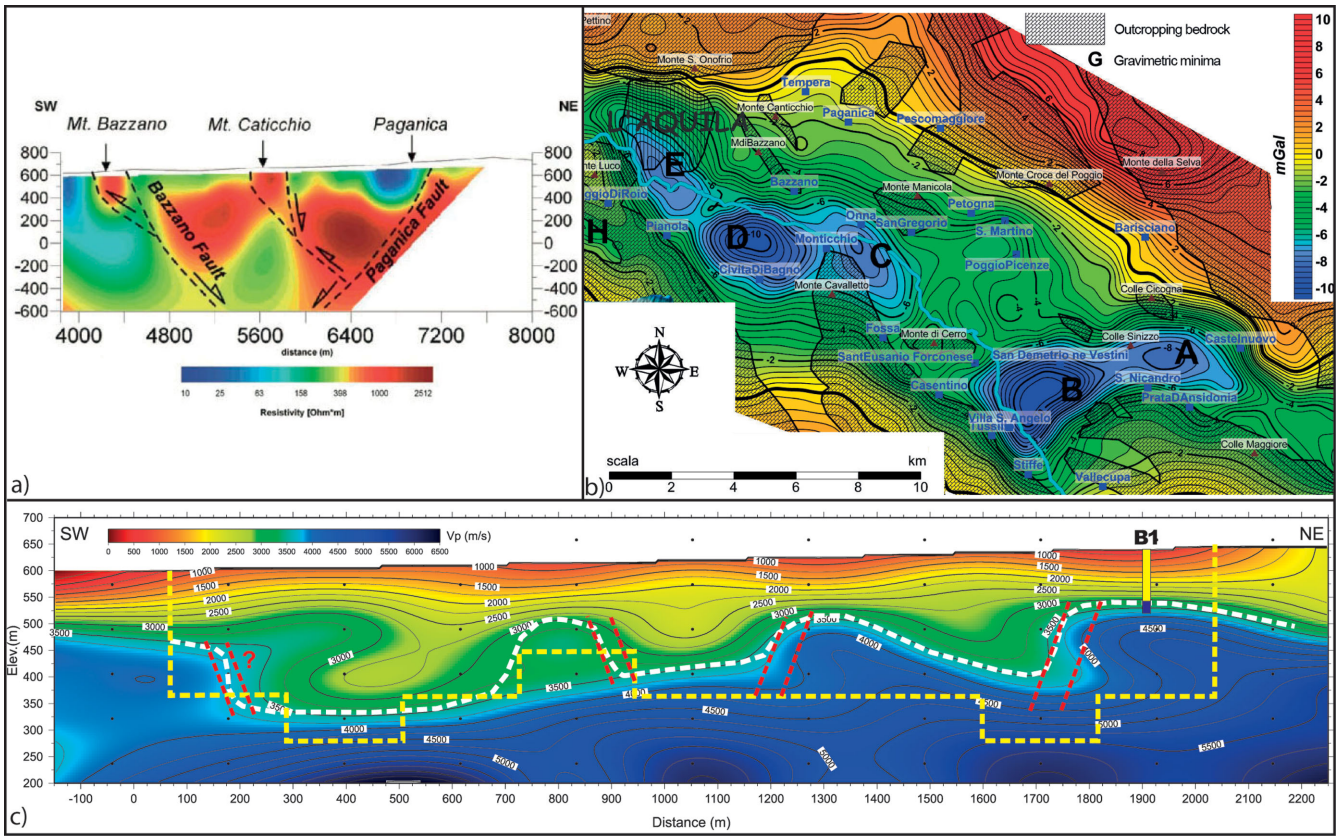

Figure 4. (a) Eastern part of the ERT resistivity profile crossing the Paganica-San Demetrio Basin interpreted by Balasco *et al*. (2011). The 200–500 Ω m value represents the bedrock/basin infill boundary. (b) Residual gravimetric anomaly map of the Middle Aterno Valley by Cesi *et al*. (2010). (c) High-resolution Vp model of seismic line P2 after Improta *et al*. (2012). Dashed lines indicate: inferred fault zones (red); resolution depth (yellow); bedrock/basin infill limit (white). The yellow/black vertical bar at the distance 1900 m shows the bedrock/basin infill limit according to the borehole B1 used for calibration. See Fig. 2 for locations.

Table 1. Main characteristics of the DERT profiles.

DERT profiles name	Profile length (m)	Maximum investigation depth (m)	# Electrodes	Configuration	Number of datum points after filtering/total data	Data deleted (%)	Max. injected current (mA)	RMS error (%)
DERT1 (A–A′) Paganica	2520	400	64	Wenner alpha	408/472	13.6	200	9.7
DERT2 (B–B′) Petogna	6360	400	160	Wenner alpha	1593/1879	15.2	500	5.6
		750		Pole–dipole	5908/6348	6.9	500	15.1
DERT3 (C–C′) San Demetrio	3800	400	96	Wenner alpha	1682/1700	1.1	500	7.9
		750		Pole–dipole	2794/3182	12.2	500	15.7

cables, a major concern is to find a compromise between signal to noise ratio and investigation depth. Wenner-alpha configuration was chosen in order to obtain the best signal/noise ratio, whereas pole–dipole configuration were performed in order to double the depth of investigation of Wenner-alpha configuration and reach ∼750 m of depth without losing too much resolution. In order to minimize the difference in using different configuration (Wenner and pole–dipole), with different sensitivity, the pole–dipole protocol has been written thanks to X2IPI software in order to optimize the 2-D imaging survey with the strategy proposed by Stummer *et al*. (2004), Wilkinson *et al*. (2006) and Alfouzan *et al*. (2010). The pole–dipole protocol used benefits of one remote electrode C2 placed with an average angle of 40 degrees from the in-line electrodes (C1 for the current injection electrode along the profile; Razafindratsima & Lataste 2014). The remote electrode C2 was installed at up to 10 km requiring a large logistical effort for the cable connection unroll and set up. In order to optimize the contact of remote electrode with the soil, we used 4 electrodes linked together. As the effect of the C2 electrode is approximately proportional to the square of ratio of the C1–P1 distance to the C2–P1 distance (P standing for potential electrode), this location meets the theoretically acceptable largest distance (five times the C1–P1 distance) in order to consider that the error caused by neglecting the effect of the C2 electrode is <5 per cent (Loke 2011). Since the exact error also depends on the location of the C2 electrode, the exact geometric factor was also introduced into the inversion in order to compare this effect. This operation gave a benefit of 6 per cent on the final RMS error.

Salty water enhanced the galvanic contact of the electrodes with the ground. As a result for 75 per cent of the measurements the contact resistance was in the 115–550 Ω range. Such low contact resistances is required to inject into the ground enough current (500 mA), necessary to get a good signal-to-noise ratio (Finizola *et al*. 2006; Revil *et al*. 2008; Barde-Cabusson *et al*. 2009). The impulse duration was set up to 0.9 s, with 0.9 s between each

current injection, and the data stacking level was adjusted to 5 per cent of median, with a maximum of 6 stacks.

An optimized 'roll along' protocol allowed to reduce the acquisition time for both Wenner-alpha and pole–dipole arrays. The multichannel pole–dipole protocol programmed into the Terrameter was specifically written in order to optimize the array geometric factor.

We included topography information in the apparent resistivity data files. We located electrodes using a handheld Garmin GPS with a horizontal accuracy ∼3 m and their elevation was obtained from a 1 m resolution DEM derived from airborne LiDAR (Light Detection And Ranging).

3.2 Data processing for resistivity measurements

We processed apparent resistivity data using ABEM utilities software for converting data format and X2IPI software (Robain & Bobachev 2002) for data filtering, while data inversion was carried out with RES2DINV software (Loke & Barker 1995). This code uses a finite element grid for the forward modelling of the voltage response to current injection. RES2DINV is based on a finite element (nonlinear) forward operator used to compute the predicted electrostatic potential distribution dp for a given resistivity model m: $dp = K(m)$. An estimated model can be retrieved from the data using the inverse operator $K{-}1$: $me = K{-}1(d0)$ where me is the estimated resistivity model based on the observed electrostatic potential distribution $d0$. RES2DINV is based on a Gauss–Newton approach with an L2 norm data misfit function.

The entire data processing workflow can be subdivided in different steps and includes: (1) conversion of raw data (binary) into ASCII format compatible data; (2) analysis of DC potentials versus standard deviation of each data set with an Excel routine (see Fig. A in the Supporting Information). This procedure allows to identify (i) some equipment problems (cable isolation, SP removal on the resistivity-meter) causing strange values, (ii) too low (or too high) potential datum points, and (iii) noisy datum points (above a standard deviation level); (3) based on the last analysis, suppression using X2IPI (Robain & Bobachev 2002) of the anomalous points with DC potential lower than 0.001 Volt or standard deviation above 5 per cent (see Fig. A in the Supporting Information DR1); (4) concatenation of main and roll-along acquisitions (including forward and reverse acquisitions for the pole–dipole array); (5) introduction of the exact geometric factor for remote electrode location for the pole–dipole array; (6) introduction of topography into data set; (7) inversion of apparent resistivity data through a linearized least-squares algorithm to obtain true resistivity sections (Loke & Dahlin 2002).

For the three profiles, the filtering process above-mentioned led to suppress 13.6 per cent of the data for Wenner alpha profile AA′, 15.2 per cent and 6.9 per cent for profile BB′ for Wenner alpha and pole–dipole respectively, and 1.1 and 12.2 per cent for profile CC′ for Wenner alpha and pole–dipole, respectively (see Table 1). The parameters used for the RES2DINV inversion process do not tend to influence the model to any specific geological structure geometry (see supplementary material DR2).

4 RESULTS: 2-D RESISTIVITY MODELS

The RMS errors of our profiles are 9.7, 5.6, 15.1, 7, 9 and 15.7 per cent respectively for A–A′ (Wenner-alpha configuration), B–B′ (Wenner-alpha and pole–dipole configuration) and C–C′ (Wenner-alpha and pole–dipole configuration) profiles. For the three profiles, 99 per cent of the true resistivity data are located between 10 and 4000 Ω m.

Surface geological data such as distribution of depositional units, location of fault traces and fault dip angle (∼60°; Fig. 2), along with lithostratigraphic characteristics (Fig. 3) was included into the qualitative interpretation and resulted determinant in this step of analysis. Notably, most of the main lateral discontinuities of resistivity coincide with lateral changes of lithology due to tectonic contacts by means of outcropping normal faults, and the thickest low ρ-regions match the zones of their hanging wall. This points out a remarkable positive correlation with the continental infill.

The comparison between outcropping geological units and lateral resistivity transition suggested the range 250–350 Ω m as the interface between the Pre-Pliocene bedrock and the Plio-Quaternary deposits (yellow in the resistivity colour scale of Figs 5–7).

Moreover, we also applied another approach to better assess the range of values corresponding to the boundary between the Pre-Pliocene bedrock and the Plio-Quaternary deposits: We tested on the true resistivity values the probability plot technique (Sinclair 1974). This approach performed on each ERT profile, displays two main geological bodies on the basis of their electrical conductivity (one inflection point). A–A′ and C–C′ profiles display one inflection point (see black arrows in Supporting Information DR3), and no evidence of inflection point for B–B′ profile. The inflection area is located between 244 (A–A′ profile) and 400 Ω m (C–C′ profile). This range of resistivity (yellow and brown colours for the three resistivity profiles) can be related to the interface between the Pre-Pliocene bedrock and the Plio-Quaternary deposits. Similar values were interpreted as bedrock/basin infill interface also by Boncio *et al*. (2011), Giocoli *et al*. (2011) and Villani *et al*. (2015), performing shallow, high-resolution ERT investigations calibrated by palaeoseismological trenches and boreholes data (Gruppo di Lavoro MS–AQ 2010), as well as Balasco *et al*. (2011; see Fig. 2 for locations). However, we are aware that the electrical resistivity of carbonates may span two orders of magnitude or even more, due to the complex interactions between porosity, degree of saturation and connectivity of fractures (Sen 1997; Jackson *et al*. 2002; Jouniaux *et al*. 2006). For these reasons, low-resistivity values ($\rho < 250$ Ω m) can correspond to saturated carbonates and marly limestones, while $\rho > 400$ Ω m can be associated with highly cemented conglomerate or breccia. Also, Zhou *et al*. (2002) and Tassy *et al*. (2014) report results of ERT investigations in karstic carbonate aquifers, and they interpret regions with $\rho <$ 200–300 Ω m as clay-filled conduits or densely fractured and saturated carbonates. Furthermore, within the Plio-Quaternary cover, we relate very low ρ values (<40 Ω m) to silty sands and clays, while slightly higher values ($\rho > 90$ Ω m) to deposits rich in conglomerates.

The acquisition and comparison of the inversion results of both configurations (Wenner-alpa and pole–dipole) for the central and southern profiles was a useful instrument to verify possible 3-D effects. The two models in general agree and show, in a first order, the same location and depth of the resistivity bodies, suggesting that the influence of lateral 3-D effects is limited. In the following, we present only the Wenner-alpha model for ERT1 and ERT2, and pole–dipole model for ERT3, while the ERT2 pole–dipole and the ERT3 Wenner-alpha are contained in the Supporting Information (DR4).

Fig. 5(a) shows the ERT1 model of the northern profile (A–A′). Its main features are: (1) low-resistivity ($\rho < 70$ Ω m) regions, ∼100–200 m wide, that reach ∼40–60 m in depth in the western part of the section (x = 350–850 m); (2) shallower low-resistivity

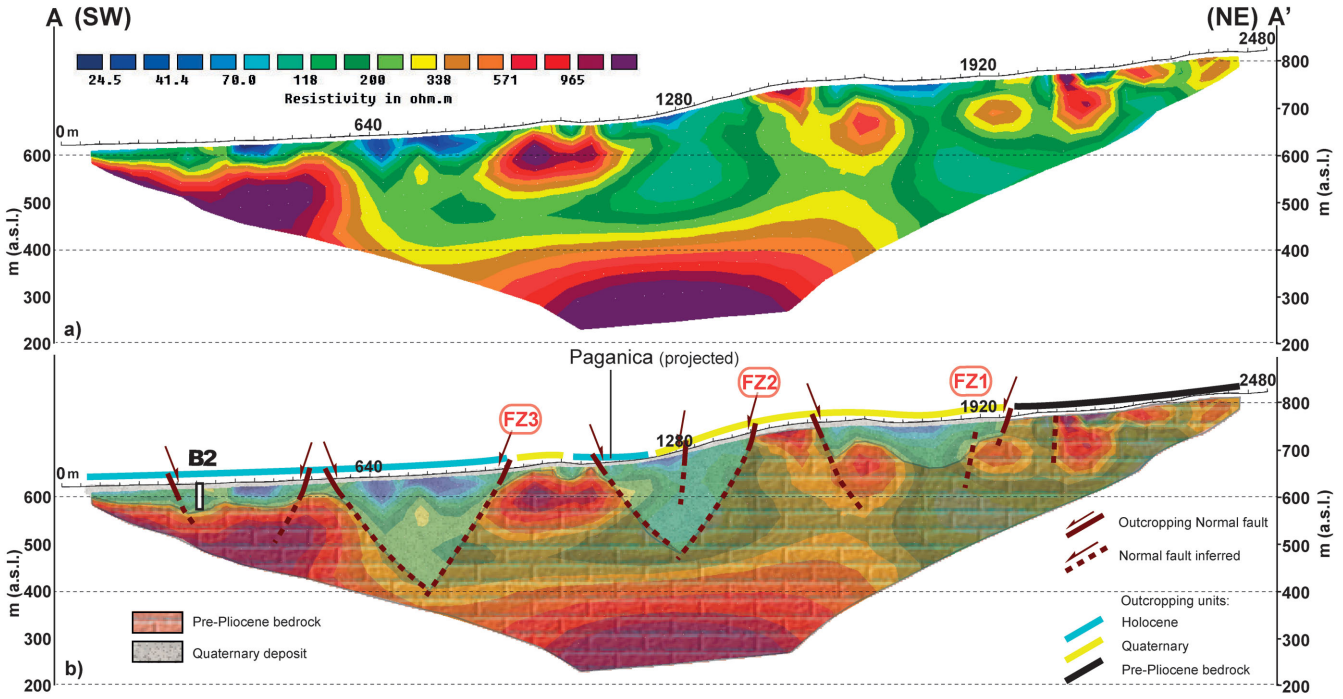

Figure 5. (a) ERT1 model (Wenner alpha); (b) ERT1 interpretation of the tomographic image with the bedrock/basin infill bodies highlighted. The main depositional units and fault zones (dip angle ~60°) mapped at the surface are reported. Borehole B2 (white box) that drills a minimum of 50 m of alluvial deposits is shown. The 250–400 Ω m resistivity value sets the limit between the two main depositional units. Dark red lines indicate faults from Pucci *et al.* (2015) that find expression on the tomographic image. See Fig. 2 for locations.

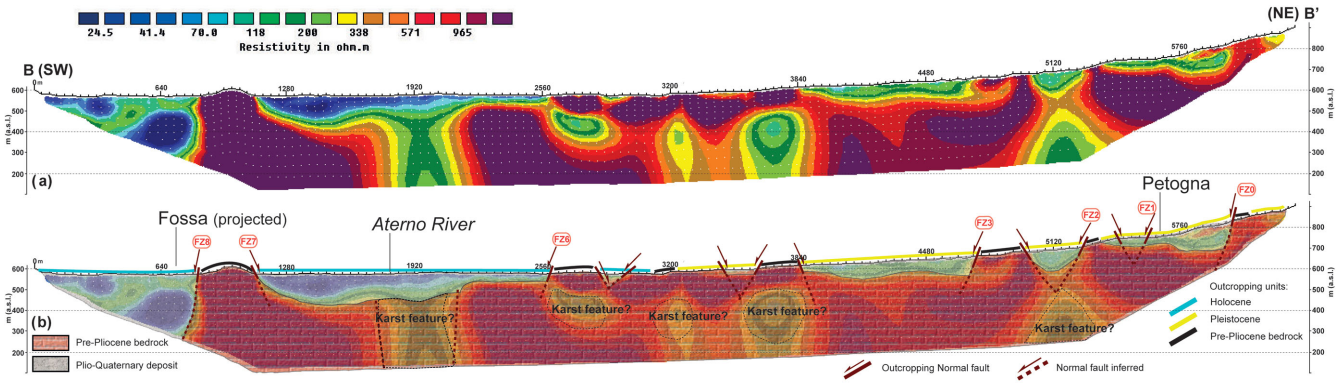

Figure 6. (a) ERT2 model (Wenner alpha); (b) ERT2 interpretation of the tomographic image with the bedrock/basin infill bodies highlighted. The main depositional units and fault zones (dip angle ~60°) mapped at the surface are reported. The 250–400 Ω m resistivity value sets the limit between the two main depositional units. Dark red lines indicate faults from Pucci *et al.* (2015) that find expression on the tomographic image. See Fig. 2 for locations.

(ρ < 100 Ω m) regions at the topographic scarp (x ~ 1280 m) and on the upper surface (x ~ 1800 m); (3) shallow high-resistivity bodies (ρ > 500 Ω m) at the western part of the profile (x = 0–600 m), at the base of the topographic scarp (x ~ 1000 m); (4) lateral resistivity changes that reach 200 m in depth, showing sub-vertical discontinuities at x = 640, 900, 1120, 1440 and 1900 m; 5) low-resistivity values below some of the shallow high-resistivity bodies.

Here, lateral discontinuities of resistivity coincide with faults bounding and lowering both Quaternary (FZ1) and Holocene (FZ3) infills (Fig. 5b).

The ERT2 profile (B–B′) shows as main features (Fig. 6a): (1) a ~300 m deep, low-resistivity (ρ < 100 Ω m) region along the SW part of the profile and a shallower low-resistivity area (ρ < 80 Ω m, <200 m in depth) in coincidence of the Aterno River; (2) shallow low-resistivity area (<100 m in depth) along the NE part of the model; (3) high-resistivity bodies (ρ > 500 Ω m), generally confined by large resistivity gradients, which are shallow or even outcropping at x ~ 1000 m and x = 2600–3840 m; (4) a sharp, vertical discontinuity in resistivity at the SW edge of the profile (x = 800 m) and below the Aterno River valley (x = 1920 m); (5) low-resistivity values below some of the shallow high-resistivity bodies (e.g. x = 3200 m).

Also here, remarkably, most of the low-resistivity bodies are bounded by outcropping normal faults (Fig. 6b). In particular, the sharp, vertical discontinuity at the SW edge appears as a clear tectonic contact. Reasonably, the observed resistivity inversions at depth can be imputed to karst phenomena and significant water circulation affecting the bedrock units (apart from the sharp discontinuity buried below the Aterno River, which is of uncertain interpretation), since the Mesozoic-Tertiary sequence is composed

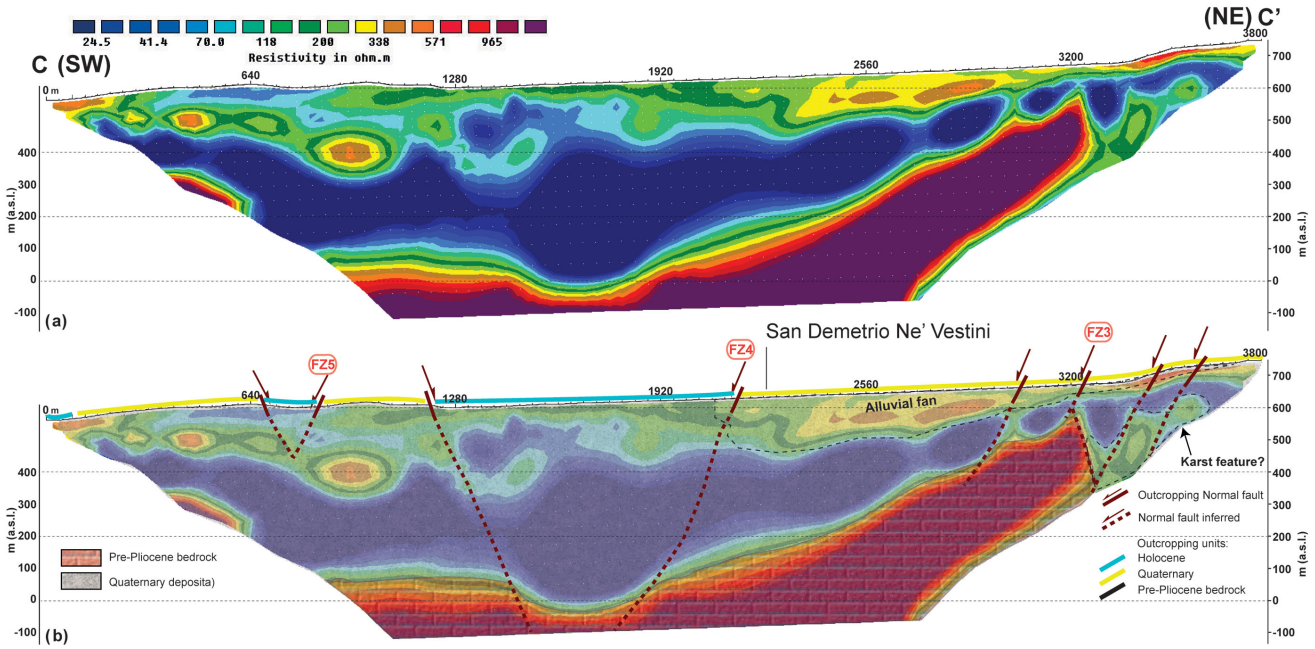

Figure 7. (a) ERT3 model (pole–dipole); (b) ERT3 interpretation of the tomographic image with the bedrock/basin infill bodies highlighted. The main depositional units and fault zones (dip angle ∼60°) mapped at the surface are reported. The 250–400 Ω m resistivity value sets the limit between the two main depositional units. Dark red lines indicate faults from Pucci *et al*. (2015) that find expression on the tomographic image. See Fig. 2 for locations.

of a continuous carbonatic and marly carbonatic lithologies of similar electrical properties.

Fig. 7(a) shows the ERT3 model of the southern profile (C–C′). Its main features are: (1) a thick, low-resistivity body ($\rho < 100$ Ω m), that reaches 600 m in depth and thins to the NE, this is overlaid by a shallow, mid-resistivity volume ($100 < \rho < 350$ Ω m), up to 200 m deep in the eastern portion of the profile; (3) a deep high-resistivity body ($\rho > 500$ Ω m) that encompasses most of the section, dips to the SW, and reaches its concave minimum at $x = 1700$ m; (4) few and smooth vertical discontinuities in resistivity affecting the shallow, moderately resistive volume in the NE and a single marked lateral discontinuity of the high-resistivity body at $x = 3200$ m.

ERT3 section (Fig. 7b), interpreted on the basis of surface geological data, highlights a thick continental infill above a deep Mesozoic-Tertiary substratum. A shallow moderately resistive volume can be attributed to the fluvio-alluvial conglomeratic facies that characterizes the top of continental infill deposits. Lateral resistivity changes can be barely ascribed to faulting and are mostly constrained by the geological mapping. A single sharp lateral resistivity change is located at $x = 3200$ m and dips northeast.

5 INTERPRETATION: THE INTEGRATED GEOLOGICAL CROSS-SECTIONS

With the aim of (1) providing an interpretation of the deep structures and their relation with the outcropping ones, and (2) imaging the geometry of the bedrock-basin infill boundary, we integrated the ERT models with the geological stratigraphic units and faults provided by Pucci *et al*. (2015). We reconstructed three cross-sections by extending the surface geological data at depth, following stratimetrical approaches and available stratigraphical columns. This was made taking into account the real attitude of units bedding and dip angles of faults measured at the surface, in order to fit the resistivity models without going beyond their resolution limit (Fig. 3).

As part of the three different marly carbonatic Mesozoic-Tertiary sequences, the Jurassic, Cretaceous-Eocene and Oligocene-Miocene formations present variable thickness (about 900–760–320 m, respectively, in the Aterno Valley-Mt. Camarda sequence; 900–560–780 m, respectively, in the Paganica sequence; 900–750–300 m, respectively, in the Mt. Pettino sequence; Fig. 3a).

Regarding the continental deposits (mainly breccia, sandy clay, conglomerate and silt), we also adopted three different stratigraphical columns from north to south: Paganica, Poggio Picenze and San Demetrio (Pucci *et al*. 2015; Fig. 3b). Overall, these show a southward increasing thickness of the fluvio-lacustrine (Early Pleistocene; SNL and VOC) and upper fluvio-alluvial (Early-Middle Pleistocene; VIC) cycles (from 70 to 280 m), along with a thickening of the Late Pleistocene alluvial fans (AFP) in the Poggio Picenze area (from 5 to 25–30 m). Where possible, we set the thickness of the Holocene fluvio-alluvial sequence and the depth of the basin infill based on published borehole logs (Gruppo di Lavoro MS–AQ 2010; Fig. 2). We therefore assume by default that the continental infill imaged by the ERT models is composed at depth by the complete, pertinent stratigraphic sequence, complying with the constraints from surface data and ERT models.

On these integrated geological cross sections, we calculated the cumulative and the Quaternary throws (i.e. measuring the vertical separation of the top of the Mesozoic-Tertiary sequences and the bottom of the Quaternary infill cut-off, respectively). The spatial resolution of our models (40 m electrodes spacing and 20 m grid for the inversion of resistivity data) allows only the recognition of those faults with displacements >>20 m. To take into account this resolution limit, we rounded the displacement estimates to multiples of 50 m.

The ERT1 integrated geological cross-section shows three main fault zones characterized by SW-dipping leading normal faults from which NE-dipping, antithetic faults splay out (Fig. 8). This structural style defines grabens, which acted as sedimentary traps for the continental sequence, and horsts made of carbonatic

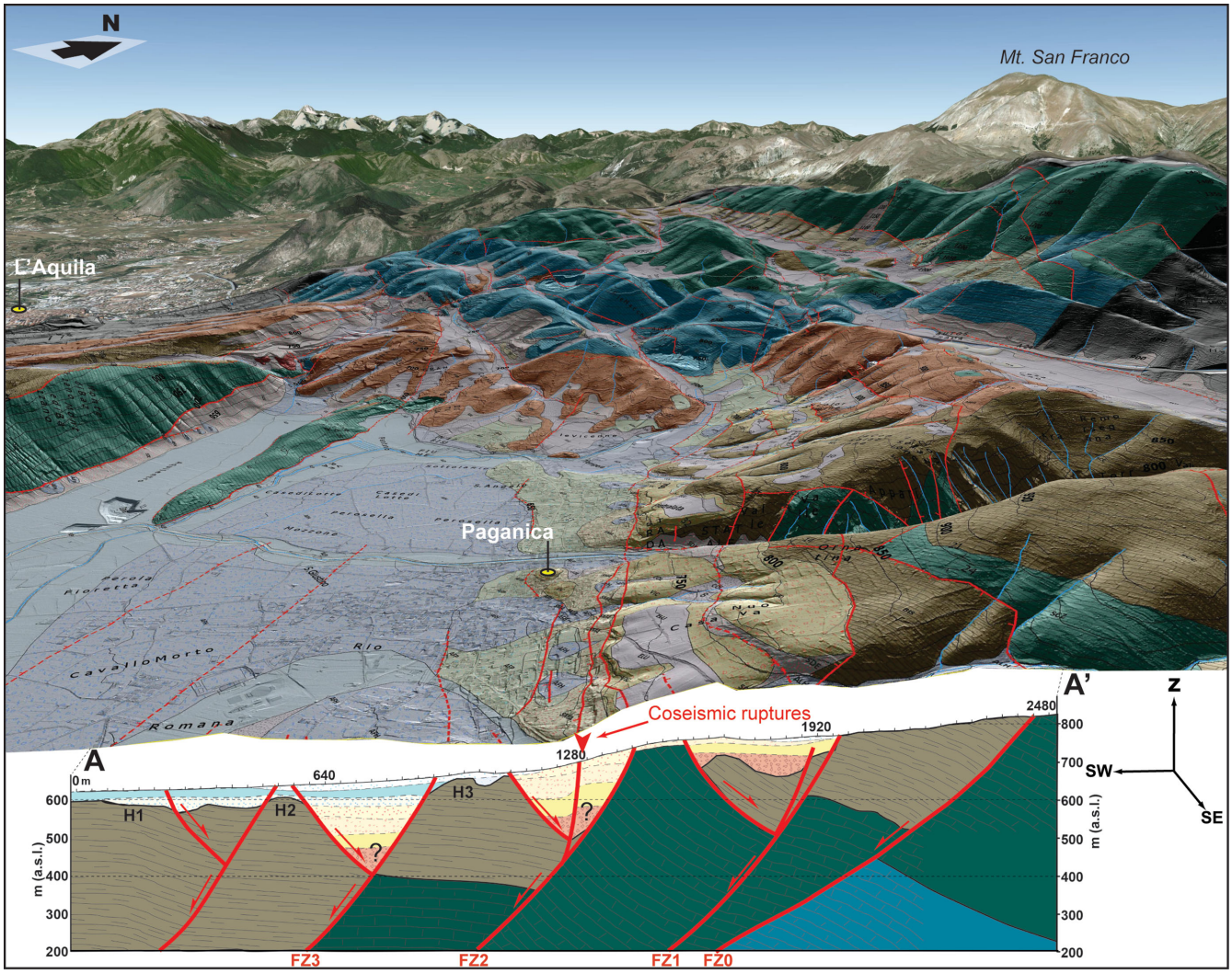

Figure 8. Block diagram of ERT1 integrated geological cross-section. Red arrow points to the location of 2009 coseismic surface ruptures. See Fig. 3 for legend of the stratigraphic sequences and Fig. 2 for location.

substratum heights. Fault zone 0 (FZ0) dips SSW and does not control continental deposits. FZ1 bounds a shallow graben (<100 m thick) hanging >100 m over the present alluvial plain with a top flat land surface. Here, old alluvial conglomerates (VIC) are exhumed due to footwall uplift. FZ2 bounds a deep graben (>150 m thick), and is also responsible for a prominent topographic scarp and exposes younger alluvial silts deposits (SMA). FZ3 bounds a depocentre (>200 m thick) that we infer to be filled with the complete Quaternary continental sequence. On the basis of the substratum interpretation (contact Cretaceous-Eocene Fm./Oligocene-Miocene Fm.), the fault zones FZ0, FZ1, FZ2 and FZ3 present total cumulative throws of ~300, ~100, >350 and >200 m, respectively (Figs 2 and 8). The same fault zones present Early Pleistocene cumulative throws of 0, ~100, ~150, ~100 m (calculated by the offset of the bottom VIC). Another feature standing out in this profile is the presence of three prominent shallow substratum heights (H1, H2, H3), flanked by faults that are buried under thin Quaternary cover (<50 m).

The ERT2 integrated geological cross-section shows a series of SW-dipping faults forming an overall staircase setting in the bedrock, with localized horst and graben controlled by antithetic faults. A thick continental Quaternary infill (up to 300 m) is located mainly in the SW part of the section, where the Holocene depocentres occur (Fig. 9). FZ6 and FZ8 show an important offset of unknown Quaternary stratigraphic units (100 and >200 m, respectively) comparable to the bedrock offset, whereas the bounding, NE-dipping fault zones (FZ7 and FZ9) present large cumulative throws (up to 500 m). Conversely, along the central part of the profile, most of the fault zones controls shallow Middle-Late Pleistocene basins (~100 m thick along theFZ2 and FZ3; <50 m thick along the FZ1 and between FZ6 and FZ3, measuring the offset of the SMA bottom cut-off) characterized by comparable cumulative throws. Along the NE edge of the cross-section, the SW-dipping FZ0 shows a cumulative throw >300 m, half of which has accumulated during whole Quaternary as shown by the 150 m thick Early Pleistocene infill (measuring the offset of the VVB top cut-off), which hangs >200 m over the plain.

The ERT3 integrated geological cross-section (Fig. 10) shows the SW- and NE-dipping FZ4 and FZ5 with a cumulative throw of the substratum (~100 m) slightly larger than the Early-Middle Pleistocene one (~50 m, measuring the offset of the VIC top cut-off). Conversely, the SW-dipping FZ3, clearly constrained by the geological mapping, presents a minimum cumulative throw of ~300 m (measuring the offset of the Jurassic Fm. top cut-off), that is

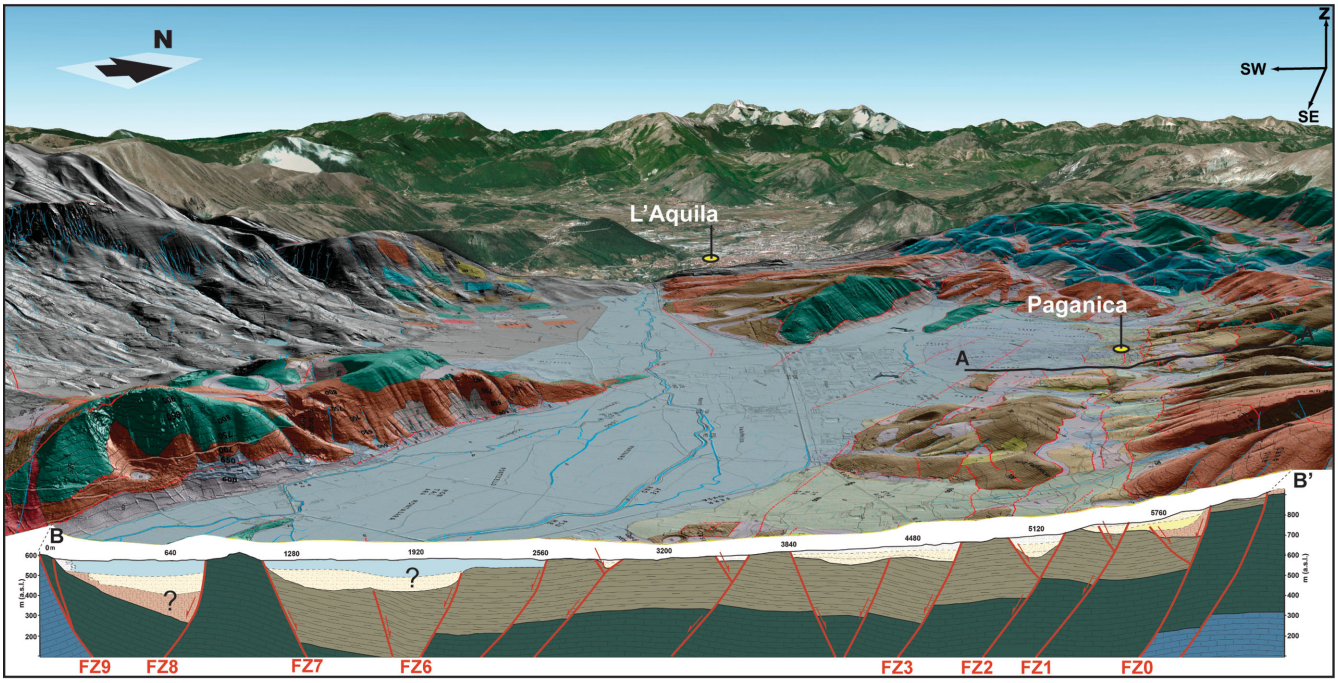

Figure 9. Block diagram of ERT2 integrated geological cross-section. See Fig. 3 for legend of the stratigraphic sequences and Fig. 2 for location.

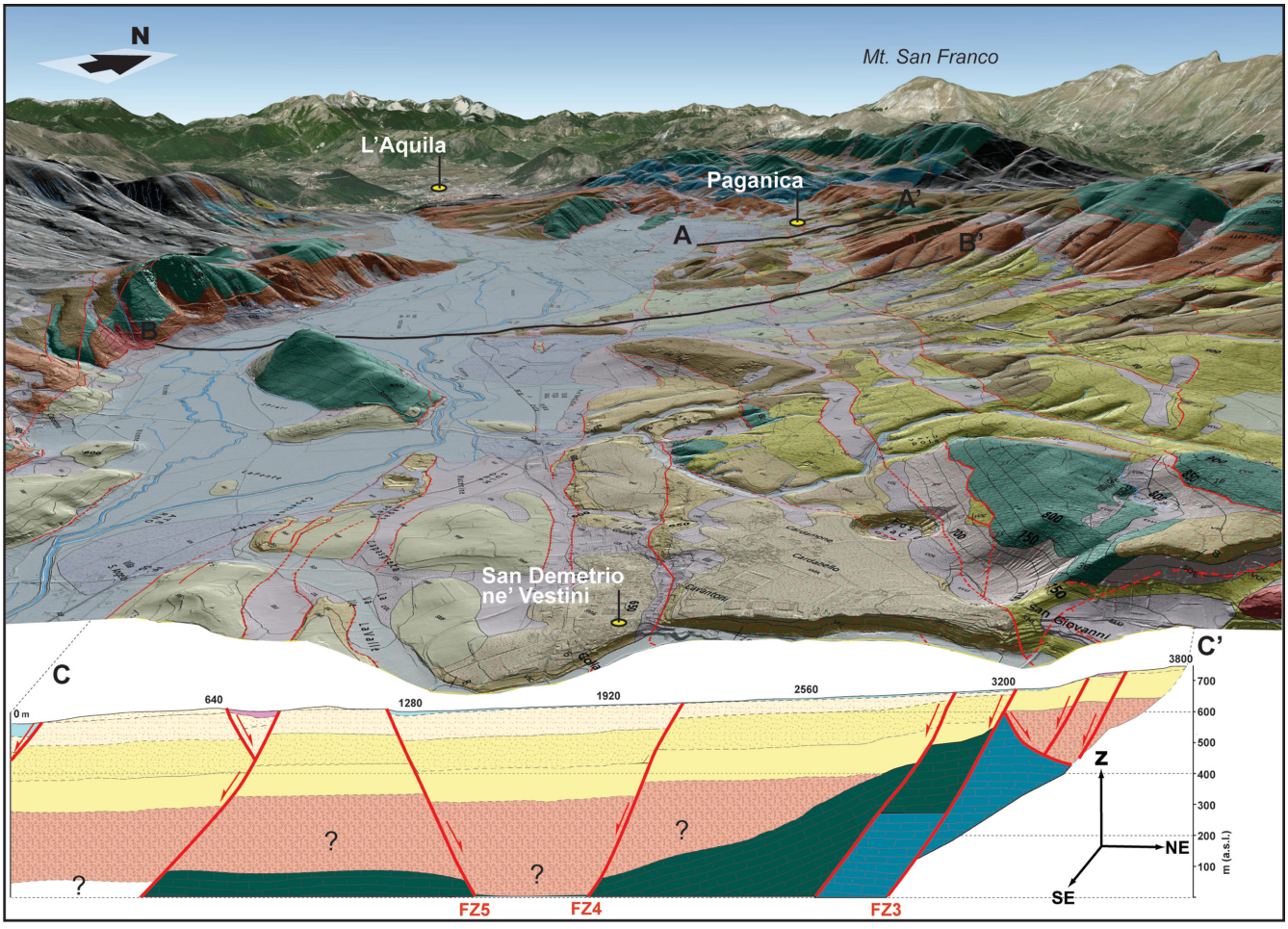

Figure 10. Block diagram of ERT3 integrated geological cross-section. See Fig. 3 for legend of the stratigraphic sequences and Fig. 2 for location.

much larger than the 150 m Quaternary throw (measuring the offset of the SNL top cut-off). The steep-sloping basin bottom between $x = 1920$ m and $x = 3200$ m can be due to a series of staircase faults that progressively lower the bedrock and that are not much resolved by the method or due to tectonic tilting. The NE-dipping vertical discontinuity at $x = 3200$ m matches the projection of a nearby E–W trending fault detected in the field that appears to be cut by FZ3. The ERT3 differs substantially from the others as it reveals the presence of the deepest Quaternary depocentre in the basin that reaches up to 600 m. Given the constraint of the upper Early Pleistocene alluvial deposits (VIC) outcrops and assuming the infill being composed by the complete continental sequence with the largest known thickness, we observe that: (1) the total thickness of the conglomeratic sequences well match the shallow moderately resistive volume reaching 150 m depth; (2) the lowermost part of the depocentre, filled by low-resistivity deposits, is deeper than the known aggregate thickness of the oldest continental units of the sequence (i.e. lacustrine –SNL– or saturated conglomerate/breccia –VVB/VVC, 400 m thick).

6 DISCUSSION AND SPECULATIONS

On the basis of the subsurface images of the Paganica-San Demetrio Basin obtained by the three integrated ERT profiles, it is possible to speculate on the location and activity of the main splays of the PSDFS, on the basin infill history and on the estimate of the slip rates. Taking into account the capabilities and limitations of the provided resistivity model especially at great depth, we attempt a comparison between the long and the short-term expressions, useful to give a complete insight on the seismic potential of the 2009 seismic source.

6.1 The basin-bottom geometry

The Paganica-San Demetrio Basin bottom is tectonically controlled by normal faults that are part of the PSDFS. Due to their persistent activity, some of these faults generated landforms that today are totally or partially buried below the continental basin infill. Overall, the style of the normal faulting defines a staircase lowering of the bedrock by SW-dipping leading faults from which NE-dipping, antithetic faults, splay out. Such structures deformed the bedrock basin bottom defining grabens acting as sedimentary traps and producing several continental depocentres.

Notably, the buried horst and graben setting imaged by the ERT investigations (Figs 8–10) appears to resemble the architecture of fault-parallel valleys investigated by Villani *et al*. (2015), and shown in the palaeoseismological trench walls (e.g. Cinti *et al*. 2011), pointing out a scale-independent structural style in the area.

6.2 Quaternary infill of the basin

Although only the ERT2 extends for the entire basin width, each cross-section images a general deepening of the Quaternary depocentres to the SW as due to a significant tectonic control by means of the antithetic faults.

As a whole, the Paganica-San Demetrio Basin thickens lengthwise from ∼200–300 m in the northern area to a maximum of ∼600 m to the south. This thickening is in agreement with the residual gravimetric anomaly map of Cesi *et al*. (2010; Fig. 4b) and with the observed southward thickening of the Quaternary sequences as seen from the outcrops (Fig. 3).

Notably, the maximum known thickness of the continental sequence, which is ∼400 m (Pucci *et al*. 2015), is not sufficient to fill in the main depocentre. To explain the exceeding 200 m infill we can propose three distinct alternatives: (1) a larger thickness of the Early Pleistocene continental sequence in the southern area, due to higher sedimentation rates; (2) an older age of the continental infill possibly starting already in the Pliocene; (3) the presence of a low-resistivity deposit at the base of the continental sequence, such as saturated Oligocene-Miocene deposits. Any of these possibilities implies an uneven evolution of the Paganica-San Demetrio Basin that took place mainly before the end of Early Pleistocene, and likely during the early stage of its development.

6.3 The leading faults and throw rate estimates

By means of the comparison between total and Quaternary cumulative throws it is possible to assess which are the most active fault zones that play the role of leading splays of the PSDFS.

In general, each fault exhibits the offsets increasing with depth, in agreement with the age of the deposits cut-off used for the displacement measurements. This testifies a general persistence in time of the faults activity. Conversely, FZ1 in ERT1 (Figs 2 and 8) presents the same offset for the Early Pleistocene and pre-Quaternary substratum with no involvement of the post-Early Pleistocene deposits and no tectonic scarp at the surface, suggesting an earlier activation of the fault followed by a significant reduction of activity. Moreover, fault zone FZ2 in ERT1 shows the larger cumulative throw as well as the larger Quaternary displacement, testifying its activity as leading splay. This leading splay: (1) separates a hanging wall with deep continental basins from a footwall with shallow basins and exhumed Early Pleistocene continental deposits; (2) displaces the topographic surface by generating prominent fault scarps.

Along the ERT2 (Fig. 9), FZ0 exhibits large amount of pre-Quaternary and lower part of Early Pleistocene throws with no involvement of the post-Early Pleistocene deposits and smoothed tectonic scarp, suggesting an earlier activation of the fault followed by a reduction of activity (Figs 2 and 9). Conversely, FZ2 presents the large offset of the pre-Quaternary substratum and of the post-Early Pleistocene deposits with involvement of Late Pleistocene units, suggesting a later activation of the leading fault.

Along the ERT3 (Fig. 10), FZ3 shows large pre-Quaternary and Early Pleistocene throws with a prominent tectonic scarp and appears to have been the leading fault in the past. In contrast, FZ4 and FZ5 present both low pre-Quaternary and Early-Middle Pleistocene throws, suggesting a young activation or a lower slip rate.

Summarizing, the leading fault zones for the three cross-sections appear to be: FZ2 along both ERT1 and ERT2 and FZ3 for ERT3, which in map result to be well aligned (Fig. 2).

We assume as the onset of the cumulative long-term throws the age of regional extension (∼2.5–3.0 Myr; Cavinato & De Celles 1999) and of the Quaternary throws the ages of the oldest displaced continental deposits (Pucci *et al*. 2015) along the three leading fault zones (0.9–1.2 Myr for the bottom VIC; 0.6–0.8 Myr for the bottom SMA and 0.9–1.8 Myr for the bottom VOC; Fig. 3b). We therefore calculated the following long-term and Quaternary displacement rates: 0.12–0.14 mm yr^{-1} and 0.13–0.17 mm yr^{-1}, respectively, for FZ2 along ERT1; 0.03–0.04 mm yr^{-1} and 0.13–0.17 mm yr^{-1}, respectively, for FZ2 along ERT2; 0.10–0.12 mm yr^{-1} and 0.08–0.13 mm yr^{-1}, respectively, for FZ3 along ERT3).

These values suggest that: (1) the aligned leading fault splays appear as a single fault, which accrued displacement at nearly

constant rate since the Middle Pleistocene; (2) there is a substantial stability in time of the throw rates of the leading splays at the Paganica and San Demetrio sectors, testifying a general persistence of their activity, whereas this is not the case for the Petogna sector; (3) the long-term throw rates are slightly lower than the late Pleistocene-Holocene ones obtained by shallow geophysical (0.23–0.30 mm yr^{-1}, Roberts *et al*. 2010), geological (0.4–0.9 mm yr^{-1}; Blumetti *et al*. 2013) and palaeoseismological studies (0.3–0.4 mm yr^{-1}, Cinti *et al*. 2011; ∼0.5 mm yr^{-1}, Galli *et al*. 2010; mm yr^{-1}, Moro *et al*. 2013), which may imply some short-term fluctuation of fault activity captured in the palaeoseismic record as confirmed in other areas around the world (Mouslopoulou *et al*. 2009).

6.4 The long-term versus the 2009 coseismic expressions

As highlighted also by Improta *et al*. (2012) for the northern sector of the basin (Fig. 4c), the ERT2 and ERT3 cross sections (Figs 9 and 10) show that the main presently active depocentres are located at their SW side, indicating the important and persistent role of the NE-dipping faults in controlling the continental infill of the Paganica-San Demetrio Basin. The 2009 coseismic displacement field, instead, disregards the long-term role of the NE-dipping faults, since the DInSAR fringes do not show any control on the depocentre as a result of their activity (Atzori *et al*. 2009; Fig. 1). This suggests that the 2009 seismic event cannot be considered as the 'characteristic' earthquake and that the NE-dipping faults can possibly displace the surface only during events occurring on PSDFS with $M_w > 6.1$.

Furthermore, the shift of the deformation from FZ0 to FZ2 at the ERT2 cross-section (Section 6.3) can be the evidence of a later linkage of the leading FZ2 of the Paganica sector with the FZ3 of the San Demetrio sector (Fig. 2). This hypothesis concurs to explain the subtle surface evidence of fault-related deformation between the two leading splays in the central portion of the PSDFS (close to Petogna village), as evidenced by Civico *et al*. (2015).

As consequence, in agreement with Blumetti *et al*. (2013), these linked fault splays represent the most active surface trace of the PSDFS during the Quaternary, playing a primary role in the landscape evolution of the area, despite its minor geomorphic appearance. Moreover, this linkage extends the length of the individual active fault trace beyond the 2009 coseismic surface rupture, explaining the occurrence of larger Holocene ruptures, as evidenced by palaeoseismological investigations along both Paganica and San Demetrio sectors (Cinti *et al*. 2011; Blumetti *et al*. 2015).

The long-term geomorphic expression of the basin suggests that the PSDFS ruptured also involving the whole 15 km long structure at the surface, allowing earthquakes >M 6.5 (Wells & Coppersmith 1994), besides rupturing only small sections, as it occurred in 2009.

The fault splays imaged by the ERT profiles are closely spaced and should join at quite shallow depth, becoming a unique planar fault (the 2009 April 6 seismic source) from few kilometres down to seismogenic depths (9–11 km), as also imaged by aftershocks relocation (Chiaraluce *et al*. 2011; Chiaraluce 2012; Valoroso *et al*. 2013).

7 CONCLUSIONS

We presented the results of three new ERT investigations performed across the Paganica-San Demetrio Basin in order to image the buried arrangement of the 2009 L'Aquila earthquake causative fault system (PSDFS). The three ERT were acquired with a 2.52 km long cable (64 electrodes with 40 m spacing) up to total length of 6.36 km at one profile (C–C′), obtained through several short 'roll-along', and, in one case, the combined use of a remote injection electrode that is an original application for the study of active faults. The Wenner-alpha and pole–dipole acquisitions returned resistivity values ranging from 10 to 4000 Ω m that were calibrated through surface geological data and correlated with the lithostratigraphic characteristics.

The reconstruction of the tectonic-related Quaternary basin arrangement extends at depth the image of the morphological expression of the PSDFS providing a complete insight on its long-term activity.

The employed survey configuration and technique allowed reaching the pre-Quaternary substratum up to 600 m in depth. Complex lateral and vertical heterogeneous resistivity regions suggested the existence of several tectonic features that displaced the original Meso-Cenozoic multilayer producing buried cumulative landforms and controlling the development of depressions, later filled with sequences of Plio-Quaternary continental deposits.

The geological interpretation of the tomographic images shows a structural style consisting of SW-dipping, leading normal faults from which NE-dipping, antithetic faults splay out defining grabens acting as sedimentary traps.

We observe a southeastward deepening of the Paganica-San Demetrio Basin from ∼200–300 m to the maximum depocentre of ∼600 m largely exceeding the known thickness of the continental sequence. The fact that the basin depth overtakes the maximum thickness of known outcropping Early Pleistocene units can be due to: (1) the onset of the continental deposition in the southern sector took place before the Quaternary; (2) there was an early stage of the basin development driven by different fault systems that produced a depocentre in the southern sector not related to the present-day basin shape; or (3) the fault system slip rate in the southern sector was higher than in the northern sector.

On the base of the subsurface images, it is possible to point to the location of the most active faults as leading splays of the 2009 earthquake causative fault system. Some of the recognized fault splays present large cumulative throws (>300 m) in coincidence also with a large displacement of the continental sequence (>100 m), highlighting a persistence in time of their activity.

We note a leading fault splay of the PSDFS that extends from Paganica to San Demetrio ne' Vestini as result of a post-Early Pleistocene linkage of two splays. This leading fault splay presents a constant long-term throw rate of 0.08–0.17 mm yr^{-1}, slightly lower than the late Pleistocene-Holocene rates deriving from others geological investigations, possibly due to averaging of short-term fluctuation of the fault activity.

The extension up to 15 km in length of an individual leading fault splay could explain the Holocene surface-ruptures observed by palaeoseismological investigations to be larger than those occurred during the 2009 L'Aquila earthquake.

In summary, the long-term geomorphic expression of the basin derived by the deep electrical resistivity tomography suggests that the PSDFS can also rupture involving the whole 15 km long structure, allowing earthquakes >M 6.5, besides rupturing only small sections, as it occurred in 2009.

We also underline that the methodology employing the remote electrode is a novel application for active tectonic areas and it represents an important reference for the development of similar studies everywhere. Further geoelectrical resistivity surveys in combination with other geophysical methods will be applied to get a denser

data grid and to better constrain the depth to bedrock of the Middle Aterno valley.

ACKNOWLEDGEMENTS

This work was financially supported by Project 'Fondo per gli Investimenti della Ricerca di Base (FIRB) Abruzzo: High-resolution analyses for assessing the seismic hazard and risk of the areas affected by the 2009 April 6 earthquake', No. RBAP10ZC8K_005.

REFERENCES

Alfouzan, F.A., Loke, M.H. & Nawawi, M.N.M., 2010. An evaluation of optimization strategies to automatically select the optimal set of array configurations for 2D electrical imaging surveys, *J. geophys. Int.,* **7,** 332–342.

Anzidei, M. *et al.*, 2009. Coseismic deformation of the destructive April 6, 2009 L'Aquila earthquake (central Italy) from GPS data, *Geophys. Res. Lett.,* **36,** L17307, doi:10.1029/2009GL039145.

Atzori, S. *et al.*, 2009. Finite fault inversion of DInSAR coseismic displacement of the 2009 L'Aquila earthquake (central Italy), *Geophys. Res. Lett.,* **36,** L15305, doi:10.1029/2009GL039293.

Bagnaia, R., D'Epifanio, A. & Sylos Labini, S., 1992. Aquila and subaequan basins: an example of Quaternary evolution in central Apennines, Italy, *Quat. Nova,* **2,** 187–209.

Balasco, M. *et al.*, 2011. Deep geophysical electromagnetic section across the middle Aterno Valley (central Italy): preliminary results after the April 6, 2009 L'Aquila earthquake, *Boll. Geofis. Teor. Appl.,* doi:10.4430/bgta0028.

Barde-Cabusson, S. *et al.*, 2009. New geological insights and structural control on fluid circulation in La Fossa cone (Vulcano, Aeolian Islands, Italy), *J. Volcanol. Geotherm. Res.,* **185,** 231–245.

Bertini, T. & Bosi, C., 1993. La tettonica quaternaria della conca di Fossa (L'Aquila), *Il Quaternario,* **6,** 293–314.

Blumetti, A.M., Di Manna, P., Guerrieri, L., Comerci, V. & Vittori, E., 2015. Paleoseismicity data on the San Demetrio fault (L'Aquila Basin, Central Italy), in *6th International INQUA Meeting on Paleoseismology, Active Tectonics and Archaeoseismology,* Vol. 27, pp. 55–59, eds Blumetti, A.M., Cinti, F.R., De Martini, P.M., Galadini, F., Guerrieri, L., Michetti, A.M., Pantosti, D. & Vittori, E., Miscellanea INGV, Pescina, Fucino Basin, Italy.

Blumetti, A.M., Guerrieri, L. & Vittori, E., 2013. The primary role of the Paganica-San Demetrio fault system in the seismic landscape of the Middle Aterno Valley basin (Central Apennines), *Quatern. Int.,* **288,** 183–194.

Boncio, P., Lavecchia, G. & Pace, B., 2004. Defining a model of 3D seismogenic sources for Seismic Hazard Assessment applications: the case of central Apennines (Italy), *J. Seismol.,* **8**(3), 407–425.

Boncio, P., Pizzi, A., Brozzetti, F., Pomposo, G., Lavecchia, G., Di Naccio, D. & Ferrarini, F., 2010. Coseismic ground deformation of the 6 April 2009 L'Aquila earthquake (central Italy, M_w 6.3), *Geophys. Res. Lett.,* **37,** L06308, doi:10.1029/2010GL042807.

Boncio, P. *et al.*, 2011. Geological and geophysical characterization of the Paganica-San Gregorio area after the April 6, 2009 L'Aquila earthquake (M_w 6.3, central Italy): implications for site response, *Boll. Geofis. Teor. Appl.,* **52**(3), 491–512.

Bosi, C. & Bertini, T., 1970. Geologia della media valle dell'Aterno, *Mem. Soc. Geol. It.,* **9,** 719–777.

Cavinato, G.P. & De Celles, P.G., 1999. Extensional basins in the tectonically bimodal central Apennines fold-thrust belt, Italy: response to corner flow above a subducting slab in retrograde motion, *Geology,* **27**(10), 955–958.

Centamore, E. *et al.*, 2006. *Note illustrative della Carta Geologica d'Italia alla scala 1:50.000, Foglio 359 "L'Aquila",* APAT – Servizio Geologico d'Italia e Regione Abruzzo – Servizio Difesa del Suolo, S.EL.CA., 128 pp.

Cesi, C., Di Filippo, M., Di Nezza, M. & Ferri, F., 2010. Caratteri gravimetrici della media Valle del Fiume Aterno, in *Microzonazione sismica per la ricostruzione dell'area aquilana,* 3 Vol. e Cd-rom, ed. Gruppo di Lavoro, MS–AQ, Regione Abruzzo –Dipartimento della Protezione Civile.

Cheloni, D. *et al.*, 2010. Coseismic and initial post-seismic slip of the 2009 M_w 6.3 L'Aquila earthquake, Italy, from GPS measurements, *Geophys. J. Int.,* **181**(3), 1539–1546.

Chiarabba, C., Jovane, L. & Di Stefano, R., 2005. A new view of Italian seismicity using 20 years of instrumental recordings, *Tectonophysics,* **305,** 251–268.

Chiaraluce, L., 2012. Unravelling the complexity of Apenninic extensional fault systems: a review of the 2009 L'Aquila earthquake (Central Apennines, Italy), *J. Struct. Geol.,* **42,** 2–18.

Chiaraluce, L., Valoroso, L., Piccinini, D., Di Stefano, R. & De Gori, P., 2011. The anatomy of the 2009 L'Aquila normal fault system (central Italy) imaged by high resolution foreshock and aftershock locations, *J. geophys. Res.,* **116,** B12311, doi:10.1029/2011JB008352.

Cinti, F.R. *et al.*, 2011. Evidence for surface faulting events along the Paganica fault prior to The 6 April 2009 L'Aquila Earthquake Central Italy, *J. geophys. Res.,* **116,** B07308, doi:10.1029/2010jb007988.

Cirella, A., Piatanesi, A., Tinti, E., Chini, M. & Cocco, M., 2012. Complexity of the rupture process during the 2009 L'Aquila, Italy, earthquake, *Geophys. J. Int.,* **190,** 607–621.

Civico, R., Pucci, S., De Martini, P.M. & Pantosti, D., 2015. Morphotectonic analysis of the long-term surface expression of the 2009 L'Aquila earthquake fault (Central Italy) using airborne LiDAR data, *Tectonophysics,* **644–645,** 108–121.

D'Agostino, N., Speranza, F. & Funiciello, R., 1997. Le Brecce Mortadella dell'Appennino Centrale: primi risultati di stratigrafia magnetica, *Il Quaternario,* **10,** 385–388.

D'Agostino, N., Mantenuto, S., D'Anastasio, E., Giuliani, R., Mattome, M., Calcaterra, S., Gambino, P. & Bonci, L., 2011. Evidence for localized active extension in the central Apennines (Italy) from global positioning system observations, *Geology,* **39**(4), 291–294.

Emergeo Working Group, 2010. Evidence for surface rupture associated with the M_w 6.3 L'Aquila earthquake sequence of April 2009 (central Italy), *Terra Nova,* **22**(1), 43–51.

Falcucci, E. *et al.*, 2009. The Paganica Fault and surface coseismic ruptures caused by the 6 April 2009 earthquake (L'Aquila, central Italy), *Seismol. Res. Lett.,* **80**(6), 940–950.

Finizola, A. *et al.*, 2006. Hydrogeological insights at Stromboli volcano (Italy) from geoelectrical, temperature, and CO_2 soil degassing investigations, *Geophys. Res. Lett.,* **33,** L17304, doi:10.1029/2006GL026842.

Galadini, F. & Galli, P., 2000. Active tectonics in the Central Apennines (Italy)—input data for seismic hazard assessment, *Nat. Hazards,* **22,** 225–270.

Galadini, F. & Messina, P., 2004. Early–Middle Pleistocene eastward migration of the Abruzzi Apennine (central Italy) extensional domain, *J. Geodyn.,* **37**(1), 57–81.

Galli, P., Giaccio, B. & Messina, P., 2010. The 2009 central Italy earthquake seen through 0.5 Myr-long tectonic history of the L'Aquila faults system, *Quat. Sci. Rev.,* **29,** 3768–3789.

Galli, P., Giaccio, B., Messina, P., Peronace, E. & Zuppi, G.M., 2011. Palaeoseismology of the L'Aquila faults (central Italy, 2009, M_w 6.3 earthquake): implications for active fault linkage, *Geophys. J. Int.,* doi 10.1111/j.1365-246X.2011.05233.x.

Giaccio, B. *et al.*, 2012. Fault and basin depocentre migration over the last 2 Ma in the L'Aquila 2009 earthquake region, central Italian Apennines, *Quat. Sci. Rev.,* **56,** 69–88.

Giocoli, A., Galli, P., Giaccio, B., Lapenna, V., Messina, P., Peronace, E., Romano, G. & Piscitelli, S., 2011. Electrical Resistivity Tomography across the Paganica-San Demetrio fault system (L'Aquila 2009 earthquake), *Boll. Geofis. Teor. Appl.,* **52**(3), 457–469.

Gruppo di Lavoro, MS–AQ, 2010. *Regione Abruzzo,* Dipartimento della Protezione Civile, L'Aquila, 3 vol. e Cd-rom.

Herrmann, R.B., Malagnini, L. & Munafò, I., 2011. Regional Moment Tensors of the 2009 L'Aquila Earthquake Sequence, *Bull. seism. Soc. Am.,* **101**(3), 975–993.

Hunstad, I., Selvaggi, G., Agostino, N.D., England, P., Clarke, P. & Pierozzi, M., 2003. Geodetic strain in peninsular Italy between 1875 and 2001, *Geophys. Res. Lett.,* **30**(4), 1181, doi:10.1029/2002GL016447.

Improta, L. *et al.*, 2012. High-resolution controlled-source seismic tomography across the Middle Aterno basin in the epicentral area of the 2009, M_w 6.3, L'Aquila earthquake (central Apennines, Italy), *Ital. J. Geosci.,* **131**(3), 373–388.

ISPRA, 2006. *foglio 359 L'Aquila. Carta Geologica d'Italia alla scala 1:50000,* S.EL.CA.

Jackson, P.D., Briggs, K.B., Flint, R.C., Holyer, R.J. & Sandidge, J.C., 2002. Two- and three-dimensional heterogeneity in carbonate sediments using resistivity imaging, *Mar. Geol.,* **182,** 55–76.

Jouniaux, L., Zamora, M. & Reuschlé, T., 2006. Electrical conductivity evolution of non-saturated carbonate rocks during deformation up to failure, *Geophys. J. Int.,* **167,** 1017–1026.

Lavecchia, G., Brozzetti, F., Barchi, M.R., Keller, J. & Menichetti, M., 1994. Seismotectonic zoning in east-central Italy deduced from the analysis of the Neogene to present deformations and related stress fields, *Bull. geol. Soc. Am.,* **106,** 1107–1120.

Lavecchia, G., Ferrarini, F., Brozzetti, F., De Nardis, R., Boncio, P. & Chiaraluce, L., 2012. From surface geology to aftershock analysis: constraints on the geometry of the L'Aquila 2009 seismogenic fault system, *Ital. J. Geosci.,* **131**(3), 330–347.

Loke, M.H., 2011. 'Tutorial: 2D and 3D electrical imaging surveys.' 136. Available at: www.geotomosoft.com.

Loke, M.H. & Barker, R.D., 1995. Least-square inversion of apparent resistivity pseudosections, *Geophysics,* **60,** 1682–1690.

Loke, M.H. & Dahlin, T., 2002. A comparison of the Gauss–Newton and quasi-Newton methods in resistivity imaging inversion, *J. Appl. Geophys.,* **49**(3), 149–162.

Montone, P., Mariucci, M.T. & Pierdominici, S., 2012. The Italian present-day stress map, *Geophys. J. Int.,* **189,** 705–716.

Moro, M., Gori, S., Falcucci, E., Saroli, M., Galadini, F. & Salvi, S., 2013. Historical earthquakes and variable kinematic behaviour of the 2009 L'Aquila seismic event (central Italy) causative fault, revealed by paleoseismological investigations, *Tectonophysics,* **583,** 131–144.

Mouslopoulou, V., Walsh, J.J. & Nicol, A., 2009. Fault displacement rates on a range of timescales, *Earth planet. Sci. Lett.,* **278**(3), 186–197.

Papanikolaou, I.D., Foumelis, M., Parcharidis, I., Lekkas, E.L. & Fountoulis, I.G., 2010. Deformation pattern of the 6 and 7 April 2009, $M_w = 6.3$ and $M_w = 5.6$ earthquakes in L'Aquila (Central Italy) revealed by ground and space based observations, *Nat. Hazards Earth Syst. Sci.,* **10,** 73–87.

Pucci, S. *et al.*, 2015. Quaternary geology of the Middle Aterno Valley, 2009 L'Aquila earthquake area (Abruzzi Apennines, Italy), *J. Maps,* **11**(5), 689–697.

Razafindratsima, S. & Lataste, J.-F., 2014. Estimation of the error made in Pole–Dipole Electrical Resistivity Tomography depending on the location of the remote electrode: Modeling and field study, *J. Appl. Geophys.,* **100,** 44–57.

Revil, A. *et al.*, 2008. Inner structure of La Fossa di Vulcano (Vulcano Island, southern Tyrrhenian Sea, Italy) revealed by high resolution electric resistivity tomography coupled with self-potential, temperature, and CO_2 diffuse degassing measurements, *J. geophys. Res.,* **113,** B07207, doi:10.1029/2007JB005394.

Revil, A. *et al.*, 2011. Hydrogeology of Stromboli volcano, Aeolian Islands (Italy) from the interpretation of resistivity tomograms, self-potential, soil temperature, and soil CO_2 concentration measurements, *Geophys. J. Int.,* **186,** 1078–1094.

Robain, H. & Bobachev, A., 2002. 'X2IPI Tool box for 2D DC and DC-IP measurements'. Available at: http://geophys.geol.msu.ru/x2ipi/x2ipi.html#boba.

Roberts, G.P., Raithatha, B., Sileo, G., Pizzi, A., Pucci, S., Walker, J.F. & Walters, R., 2010. Shallow subsurface structure of the 2009 April 6 M_w 6.3 L'Aquila earthquake surface rupture at Paganica, investigated with ground-penetrating radar, *Geophys. J. Int.,* **183**(2), 774–790.

Rovida, A., Camassi, R., Gasperini, P. & Stucchi, M. (eds), 2011. 'CPTI11, the 2011 version of the parametric catalogue of Italian Earthquakes, Milano, Bologna, last release 2011-12-23'. Available at: http://emidius.mi.ingv.it/CPTI, doi:10.6092/INGV.IT-CPTI11.

Santo, A., Ascione, A., Di Crescenzo, G., Miccadei, E., Piacentini, T. & Valente, E., 2014. Tectonic-geomorphological map of the middle Aterno river valley (Abruzzo, Central Italy), *J. Maps,* **10**(3), 365–378.

Scognamiglio, L., Tinti, E., Michelini, A., Dreger, D., Cirella, A., Cocco, M., Mazza, S. & Piatanesi, A., 2010. Fast determination of moment tensors and rupture history: what has been learnt from the April 6th 2009, L'Aquila Earthquake Sequence, *Seismol. Res. Lett.,* **81**(6), 892–906.

Sen, P.B., 1997. Resistivity of partially saturated carbonate rocks with microporosity, *Geophysics,* **62**(2), 415–425.

Sinclair, A.J., 1974. Selection of threshold values in geochemical data using probability graphs, *J. Geochem. Explor.,* **3**(2), 129–149.

Stummer, P, Maurer, H. & Green, A.G., 2004. Experimental design: electrical resistivity data sets that provide optimum subsurface information, *Geophysics,* **69**(1), 120–139.

Tassy, A., Maxwell, M., Borgomano, J., Arfib, B., Fournier, F., Gilli, E. & Guglielmi, Y., 2014. Electrical resistivity tomography (ERT) of a coastal carbonate aquifer (Port-Miou, SE France), *Environ. Earth Sci.,* **71,** 601–608.

Tertulliani, A., Rossi, A., Cucci, L. & Vecchi, M., 2009. L'Aquila (Central Italy) earthquakes: the predecessors of the April 6, 2009 event, *Seismol. Res. Lett.,* **80**(6), 972–977.

Trasatti, E., Kyriakopoulos, C. & Chini, M., 2011. Finite element inversion of DInSAR data from the M_w 6.3 L'Aquila earthquake, 2009 (Italy), *Geophys. Res. Lett.,* **38,** L08306, doi:10.1029/2011GL046714.

Valoroso, L., Chiaraluce, L., Piccinini, D., Di Stefano, R., Schaff, D. & Waldhauser, F., 2013. Radiography of a normal fault system by 64 000 high-precision earthquake locations: The 2009 L'Aquila (central Italy) case study, *J. geophys. Res.,* **118,** 1156–1176.

Vannoli, P., Burrato, P., Fracassi, U. & Valensise, G., 2012. A fresh look at the seismotectonics of the Abruzzi (Central Apennines) following the 6 April 2009 L'Aquila earthquake (M_w 6.3), *Ital. J. Geosci.,* **131**(3), 309–329.

Vezzani, L. & Ghisetti, F., 1998. *Carta Geologica dell'Abruzzo, Scala 1:100 000,* S.EL.CA..

Villani, F. *et al.*, 2015. Imaging the structural style of an active normal fault through multi-disciplinary geophysical investigation: a case study from the M_w 6.1, 2009 L'Aquila earthquake region (central Italy), *Geophys. J. Int.,* **200**(3), 1676–1691.

Vittori, E. *et al.*, 2011. Surface Faulting of the 6 April 2009 M_w 6.3 L'Aquila Earthquake in Central Italy, *Bull. seism. Soc. Am.,* **101**(4), 1507–1530.

Volpe, M., Piersanti, A. & Melini, D., 2012. Complex 3-D Finite Element modelling of the 2009 April 6 L'Aquila earthquake by inverse analysis of static deformation, *Geophys. J. Int.,* **188,** 1339–1358.

Walters, R.J. *et al.*, 2009. The 2009 L'Aquila earthquake (central Italy): a source mechanism and implications for seismic hazard, *Geophys. Res. Lett.,* **36,** L17312, doi:10.1029/2009GL039337.

Wells, D.L. & Coppersmith, K.J., 1994. New empirical relationships among magnitude, rupture length, rupture width, rupture area, and surface displacement, *Bull. seism. Soc. Am.,* **84**(4), 974–1002.

Wilkinson, P.B., Meldrum, P.I., Chambers, J.E., Kuras, O. & Ogilvy, R.D., 2006. Improved strategies for the automatic selection of optimized sets of electrical resistivity tomography measurement configurations, *Geophys. J. Int.* **167,** 1119–1126.

Zhou, W., Beck, B.F. & Adams, A.L., 2002. Effective electrode array in mapping karst hazards in electrical resistivity tomography, *Environ. Geol.,* **42**(8), 922–928.

SUPPORTING INFORMATION

Additional Supporting Information may be found in the online version of this paper:

The file includes text and figures that are divided into three data repository items:

Data repository Item DR1: DC potentials versus standard deviation for data filtering process.

Figure A. This example shows the analysis made with Excel routine for one of our data set (first Wenner-alpha acquisition of A–A′ profile) in order to highlight DC potentials versus standard deviation. Note that stacking parameters were adjusted during the field data acquisition to 5 per cent of the median of stacked values. The following step consists using X2IPI (Robain & Bobachev 2002) in deleting all the points with a DC potential <0.001 V and all the points with a standard deviation >5 per cent (on left side of the vertical red line and above the horizontal red line, respectively).

Data repository Item DR2: IVP file with parameters used for Wenner-alpha and pole dipole inversion.

Data repository Item DR3: Probability plot technique on the true resistivity values of the 3 ERT profiles.

Figure B. Probability plot technique on the true resistivity values for the three ERT profiles. The curves of probability plot display one inflection point that indicates two main geological bodies with distinct electrical resistivity properties. A–A′ and C–C′ profiles display one inflection point (see black arrows), and no evidence of inflection point for B–B′ profile. We took for both curves, the most obvious changes in the slope (considering derivative and second derivative) of the curves. The inflection area is located between 244 (A–A′ profile) and 400 Ω m (C–C′ profile), separating the higher resistive body (Pre-Pliocene bedrock) from the lower resistive body (Plio-quaternary deposit). The range of 244–400 Ω m is nearly the same value for profiles made in different years and seasons. Moreover, this change of resistivity coincides to the lithological transition observed at surface (see Sinclair 1974 for details).

Data repository Item DR4: Comparison between Wenner-alpha and pole-dipole resistivity models of ERT2 and the ERT3.

Figure C. ERT2 model with Wenner-alpha (above) and pole–dipole (below) resistivity model. The white lines at about 338 Ω m (between yellow and brown colour) highlight the limit between bedrock and basin infill bodies for the Wenner-alpha resistivity model. The same limits were reported on the pole–dipole resistivity model. The range 250–400 Ω m between these two main depositional units was defined thanks to the probability plot technique (see DR3). See Fig. 2 for locations.

Figure D. ERT3 model with Wenner-alpha (above) and pole–dipole (below) resistivity model. The white lines at about 338 Ω m (between yellow and brown colour) highlight the limit between bedrock and basin infill bodies for the Wenner-alpha resistivity model. The same limits were reported on the pole–dipole resistivity model. The range 250–400 Ω m between these two main depositional units was defined thanks to the probability plot technique (see DR3). See Fig. 2 for locations.

(http://gji.oxfordjournals.org/lookup/suppl/doi:10.1093/gji/ggw308/-/DC1).

Please note: Oxford University Press is not responsible for the content or functionality of any supporting materials supplied by the authors. Any queries (other than missing material) should be directed to the corresponding author for the paper.